Journal of Materials Science & Technology 149 (2023) 177–189

Contents lists available at ScienceDirect

Journal of Materials Science & Technology

journal homepage: www.elsevier.com/locate/jmst

Research Article

Eutectic high entropy alloy syntactic foam

Jin Meng[a,c], Yu Qiao[a,d], Tian-Wei Liu[a,c], Yuan-Yuan Tan[a,c], Fu-Hua Cao[a,c], Yan Chen[a,c], Hai-Ying Wang[a,c], Lan-Hong Dai[a,b,c,*]

[a] State Key Laboratory of Nonlinear Mechanics, Institute of Mechanics, Chinese Academy of Sciences (CAS), Beijing 100190, China
[b] State Key Laboratory of Explosion Science and Technology, Beijing Institute of Technology, Beijing 100081, China
[c] School of Engineering Science, University of Chinese Academy of Sciences, Beijing 101408, China
[d] CAS Key Laboratory of Mechanical Behavior and Design of Materials, Department of Modern Mechanics, University of Science and Technology of China, Hefei 230027, China

ARTICLE INFO

Article history:
Received 5 May 2022
Revised 10 June 2022
Accepted 2 December 2022
Available online 28 January 2023

Keywords:
Eutectic high entropy alloy
Foams
Metal matrix composites (MMCs)
Energy absorption

ABSTRACT

High-strength metallic foams have a wide range of applications in engineering as lightweight structural and energy-absorbing materials. However, it is challenging to obtain metallic foam with both good energy absorption performance and high strength. Here, we developed a novel metal matrix syntactic foam fabricated with $AlCoCrFeNi_{2.1}$ eutectic high entropy alloy and alumina cenospheres that exhibits a remarkable combination of high strength and energy absorption performance under both quasi-static and dynamic compression. The porous structure of syntactic foam fully exploits the properties of the $AlCoCrFeNi_{2.1}$ alloy matrix with a unique FCC/B2 dual-phase eutectic microstructure and thus yields exceptional performance. We discovered that this dual-phase microstructure not only provides high strength but also allows the pores to collapse in a progressive and diffusive way, which enables the formation of a high and smooth energy absorption platform. It is found that the heterogeneity between the two phases in the matrix can provide back stress strengthening, and it also induces multiple micro shear bands and microcracks as additional energy dissipation modes as the deformation proceeds. This unique mechanism ensures the strength of microstructures and makes them fracture promptly, which causes the balance of strengthening and softening on the macro scale. This work opens the avenue for developing advanced high-strength lightweight structural and energy-absorbing materials.

1. Introduction

Metallic foams possess low density, high specific strength and stiffness, as well as improved energy absorption performance. This combination of properties makes them a promising candidate for lightweight structural and energy-absorbing applications, such as lightweight beams, buoyancy materials, crash absorbers, etc. [1–7]. As a member of the metallic foam family, metal matrix syntactic foams (MMSFs) [8–11], consisting of metal matrix and hollow inclusions, usually exhibit high strength and energy absorption performance due to the reinforcement inclusions. These properties make them more suitable for applications with high strength requirements than other metallic foams.

With the development of industry, higher demands are put forward for the strength and energy absorption of MMSFs. However, as the strength increases, the energy absorption performance of MMSFs does not simply enhance [12,13], yet sometimes even deteriorates [14,15]. A good energy-absorbing material should have a sufficient stress amplitude, a wide stress platform and a smooth and even stress–strain curve to ensure that a large amount of energy can be absorbed stably at nearly constant stress [16]. In other words, it should have high strength, enormous energy absorption capacity and good energy absorption efficiency. Nevertheless, due to the strength-ductility trade-off, high-strength MMSFs achieved by solid-solution strengthening or precipitation hardening usually exhibit brittle behavior [17–19]. As a result, their stress–strain curves are unstable and accompanied by sizeable oscillations, which downgrade their energy absorption performance. Selecting ductile alloy to fabricate MMSFs can eliminate the adverse effects of brittleness, but it also introduces new problems. For one thing, some ductile MMSFs have low strength, such as pure Al

* Corresponding author at: State Key Laboratory of Nonlinear Mechanics, Institute of Mechanics, Chinese Academy of Sciences (CAS), Beijing 100190, China.
E-mail address: lhdai@lnm.imech.ac.cn (L.-H. Dai).

https://doi.org/10.1016/j.jmst.2022.12.009
1005-0302/

[15,20,21] and some Al alloy [22,23] syntactic foams, limiting the stress amplitude of the plateau region. For another, due to the excellent ductility and strain hardening ability of the matrix, ductile MMSFs often exhibit an ascending stress plateau region that reduces the energy absorption efficiency, such as steel [14,24] and CoCrFeMnNi high entropy alloy [25] syntactic foam. Therefore, it is challenging to achieve high strength, energy absorption capacity and efficiency at the same time. And the key point is to find a suitable matrix alloy. In addition to high strength, the matrix alloy is also required to have moderate ductility and strain hardening ability to avoid both abrupt brittle failure and ascending stress plateau.

During the past decade, high entropy alloys (HEAs) or complex concentrated alloys (CCAs) [26–33], a new kind of disordered alloy composed of multi-principal elements in equimolar or near-equimolar ratio, have attracted broad interest. The novel alloy design concept provides a vast composition space, making it possible to obtain alloys with various properties [34–44]. Among these alloys, there is a subgroup called eutectic high entropy alloys (EHEA) [45,46], which combines the advantages of high entropy alloys and eutectic alloys, thus having great application prospects in industrial fields. Recently, an $AlCoCrFeNi_{2.1}$ EHEA with a unique dual-phase lamellar microstructure of soft FCC and hard B2 phases was developed by Lu et al. [47–49], which achieves a good balance of high strength and ductility due to the coupling between two constituent phases [50–57]. Moreover, the $AlCoCrFeNi_{2.1}$ EHEA has good castability and fluidity [47,48], which are desirable in the infiltration process of MMSFs. And the casting flaws such as shrinkage cavity and composition segregation can also be alleviated. For the above reasons, $AlCoCrFeNi_{2.1}$ EHEA is an ideal matrix material and is expected to enable MMSF to obtain high strength and good energy absorption performance simultaneously.

In the present work, we developed a new MMSF with $AlCoCrFeNi_{2.1}$ EHEA, and the mechanical property tests confirmed our expectations. This EHEA syntactic foam exhibits an excellent combination of high strength and energy absorption performance under both quasi-static and dynamic compression. We systematically investigated the deformation mechanisms and microstructure evolution at these two strain rates using X-ray computed tomography (CT), a scanning electron microscope (SEM), and a transmission electron microscope (TEM), and revealed the underlying mechanisms of the high strength and energy absorption performance of the MMSF. These results are illuminating for the research and development of advanced high-strength energy-absorbing and lightweight structural materials.

2. Materials and methods

2.1. Materials fabrication

The $AlCoCrFeNi_{2.1}$ EHEA ingots were melted more than four times by induction melting of high-purity (99.9%) constituent elements in an inert atmosphere. As filler materials, alumina cenospheres with a diameter of 500–600 μm and a wall thickness to radius ratio $t/R = 0.13$ were applied (provided by Zhengzhou YuLi Industry Co. Ltd., China). The chemical composition of alumina cenospheres in wt.% is $Al_2O_3 \geq 99\%$, $SiO_2 \leq 0.3\%$, $Na_2O \leq 0.35\%$ and $Fe_2O_3 \leq 0.15\%$.

All EHEA syntactic foam samples were fabricated by gas pressure infiltration method [58] in an induction furnace with custom-designed devices. The infiltration procedure in detail can be found in our previous works [25,59] and will only be outlined briefly here. First, the alumina cenospheres were filled into the alumina tube which was used as a mold, and an alloy ingot was placed on the top. Both the ingot and alumina tube were put into a quartz crucible with a diameter of 14 mm and coated with boron nitride to avoid the reaction between melted alloy and SiO_2. Then the quartz tube was installed in the induction furnace and connected with the vacuum pump and the argon gas bomb. Before infiltration, the quartz crucible was evacuated to $\sim 5 \times 10^{-3}$ Pa. After that, we heated the alloy ingot and cenospheres with an induction coil surrounding the quartz crucible. First, we preheat the alumina cenospheres at low power using the induced heat generated by the graphite tube between the quartz tube and the alumina cenospheres. Preheating can decrease resistance during infiltration, help increase infiltration length, and reduce casting flaws. Afterward, we heat the alloy ingot at high power until the ingot melted and formed a seal across the circumference of the crucible. Argon gas was then introduced rapidly, and the melted alloy was pressed to infiltrate the space between the cenospheres at a pressure of 1.5×10^5 Pa. This pressure both produces sufficient infiltration length and minimizes the destruction of the cenospheres under pressure, resulting in lower density and greater porosity of the foam. Finally, the samples were furnace-cooled.

2.2. Compression tests

Quasi-static compression tests were carried out on cylindrical syntactic foam and solid $AlCoCrFeNi_{2.1}$ samples using an electronic universal testing machine (CMT 5105S) equipped with a 100 kN load-cell. Tests were performed in accordance with ISO 13314: 2011 standard [60]. Syntactic foam specimens with a diameter of 8 mm and a height of 12 mm were machined by a diamond wire saw. Solid $AlCoCrFeNi_{2.1}$ samples with a diameter of 4 mm and a height of 6 mm were machined out of the raw ingot. Before each compression test, the ends of the samples were ground by using SiC paper and lubricated by using silicone grease to minimize friction between samples and platens. At least five samples for syntactic foam and solid matrix were tested to verify the repeatability. Tests were carried out at constant crosshead speed with an initial strain rate of 10^{-3} s^{-1}. Strains were measured by an extensometer and corrected for deflection of the load frame. To investigate the deformation mechanism, we conducted the interrupted compression tests at strains of 10%, 20%, 30%, 40%, and 50% on syntactic foam samples.

The dynamic compression tests at a strain rate of about 2000 s^{-1} were conducted on a split Hopkinson pressure bar apparatus (SHPB) [61,62]. For the current tests, the bars made of high-strength 38CrNiMoV alloy steel were used. The striker bar had a diameter of 12.6 mm and a length of 400 mm, while the incident bar and transmitter bar were 1000 mm long and 12.6 mm in diameter. Cylindrical specimens of syntactic foam (ϕ6 mm × 6 mm) and solid $AlCoCrFeNi_{2.1}$ alloy (ϕ4 mm × 4 mm) were tested. At least 5 samples for each test. For syntactic foam samples, we also conducted interrupted tests at strains of 5%, 10%, 20%, and 30% using stopper rings to study the deformation mechanism at a high strain rate.

2.3. Microstructure characterization

The internal pore structure of initial and deformed samples was investigated by X-ray computed tomography (CT, Y. CT Modular-MG452). In addition, microstructural characterizations on pre- and post-deformation specimens were performed using a scanning electron microscope (SEM, Zeiss Gemini SEM 300) and a transmission electron microscope (TEM, JEOL, JEM-2100F at 200 kV). The SEM was equipped with an electron backscattered diffraction (EBSD) system and an energy-dispersive X-ray spectrometer (EDS). The samples for EBSD observation were prepared by mechanical grinding and electropolishing. A focused ion beam (FIB) instrument (FEI Helios Nanolab 600i) was used to prepare TEM samples accurately.

3. Results

3.1. Porous structure and microstructure

The density of $AlCoCrFeNi_{2.1}$ syntactic foam (ρ_{SF}) is 4.43 ± 0.08 g cm^{-3}, corresponding to a relative density of 62.6% ± 1.1% as compared with solid $AlCoCrFeNi_{2.1}$ alloy. The volume fraction of the voids ($\emptyset_V$) is 28.0 ± 1.1%, and the volume fraction of cenosphere shells ($\emptyset_C$) and matrix ($\emptyset_M$) are 21.0 ± 0.1% and 51.0 ± 1.1%, respectively. The measurement method can be found in Supplementary Information.

The macroscopic porous structure and microstructure characterizations of syntactic foam samples are presented in Fig. 1. The CT reconstructed three-dimensional (3D) image of the syntactic foam sample is shown in Fig. 1(a), and the inset is the macrograph. The cenospheres are evenly distributed in the matrix without apparent clusters, forming a homogeneous porous structure. Most pores within the cenospheres are nearly spherical, and a few are filled with molten alloy during the infiltration. Some cenospheres fragments are also visible. The SEM image (Fig. 1(b)) shows the morphology of the polished section of syntactic foam. The alumina cenospheres and EHEA matrix are tightly fitting with nearly no visible voids between them. This is attributed to the good fluidity and castability of the EHEA matrix, preventing casting flaws, like internal shrinkage, from downgrading mechanical properties. And there is no chemical reaction between the cenospheres and the matrix, which can be confirmed by the EDS elemental mapping presented in Fig. S1 in the Supplementary Information.

A careful examination of the microstructure of syntactic foam matrix was conducted by EBSD, EDS, and TEM. Fig. 1(c) and (d) shows the EBSD phase map and inverse pole figure (IPF). The $AlCoCrFeNi_{2.1}$ alloy matrix consists of FCC and B2 dual-phase and exhibits typical eutectic microstructures [48,50]. The area fractions of FCC and B2 phase measured by EBSD phase map were about 55% and 45%, respectively. As shown in Fig. 1(c), the B2 phase has two kinds of morphology, lamellae (about 2 μm thick) and irregular islands (about 2–5 μm in diameter). The detailed crystallography of the two phases is shown in Fig. 1(d). The high-angle grain boundaries are indicated by white dashed lines. In the same grain, the B2 domains have a similar crystallographic orientation, while the FCC domains exhibit two different crystallographic orientations with a misorientation angle of 60° These two kinds of variants are referred to as V1 and V2, and have a twin relationship confirmed by TEM study [55,63]. The chemical composition and elemental distribution are investigated by EDS mapping (Fig. 1(e) and Table 1). It can be seen that Al and Ni segregate in B2 phase, while Fe, Co, and Cr are rich in the FCC phase. The composition of the entire scanning area is close to the nominal composition of $AlCoCrFeNi_{2.1}$ alloy, suggesting that the infiltration process did not cause a large deviation in element contents.

We further investigated the microstructure by TEM, as shown in Fig. 2. A low magnitude bright-field image (Fig. 2(a)) shows the morphology of the FCC/B2 lamellar structure and the growth twin (V2) in FCC phase. Selected area electron diffraction (SAED) patterns of both phases are presented in Fig. 2(b) and (c). The twin relationship between FCC matrix (V1) and growth twin (V2) can be confirmed clearly in Fig. 2(b). Moreover, additional low-intensity superlattice reflections (red circles) indicate the presence of the FCC-ordered $L1_2$ phase within the FCC matrix [50,64]. To further display the characteristics of ordered $L1_2$ phases, a high-resolution transmission electron microscopy (HRTEM) image (Fig. 2(d)) was captured from the FCC phase, and the inset is the corresponding fast Fourier transformation (FFT) pattern. The $L1_2$ particles with a diameter of 2–5 nm are distributed densely and highly coherent with the FCC matrix. Fig. 2(c) is the SAED patterns of BCC-ordered B2 phase [50,64]. The bright-field TEM image (Fig. 2(e)) taken from the B2 domain indicates that the B2 phase also contains precipitate particles (pointed by yellow arrows), which have a diame-

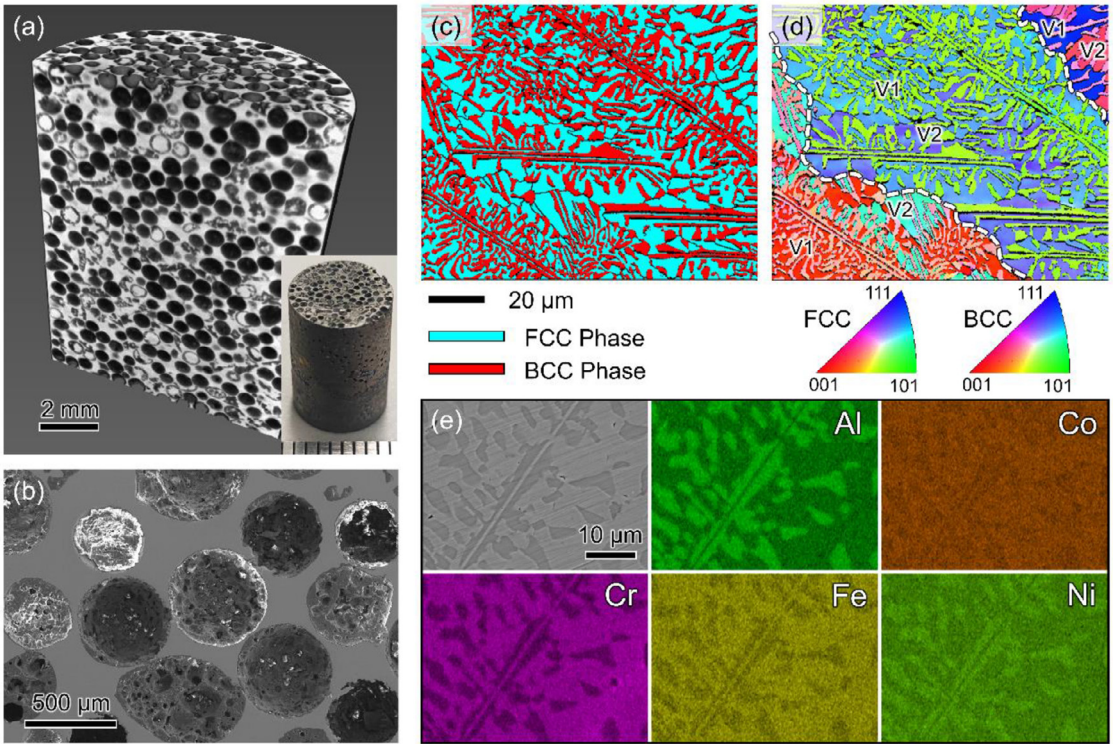

Fig. 1. The initial porous structure and microstructure characterizations of the syntactic foam sample. (a) The CT reconstructed 3D image, inset is the macrograph. (b) The SEM secondary electron image shows the morphology of a polished section. (c) The EBSD phase map and (d) inverse pole figure (IPF) of syntactic foam matrix. (e) The EDS elemental distribution maps of syntactic foam matrix.

Table 1
Chemical composition (at.%) of $AlCoCrFeNi_{2.1}$ syntactic foam matrix measured by EDS.

Phase	Al	Co	Cr	Fe	Ni
FCC	11.21 ± 0.36	18.84 ± 0.06	19.45 ± 0.22	19.45 ± 0.36	31.07 ± 0.28
B2	28.70 ± 0.75	13.29 ± 0.29	9.14 ± 0.20	10.97 ± 0.28	37.92 ± 0.02
Whole area	17.54	16.76	16.15	16.32	33.24

ter of 20–40 nm. These precipitates produced additional satellite reflections in SAED patterns [64] (marked with yellow arrows in Fig. 2(c)). Fig. 2(f) shows the zoom-in image of these particles, and the inset is the HRTEM image of the frame area. Literature reports [50,64] suggest that these particles are Cr-rich BCC phases and may be formed via spinodal decomposition of B2 phase during solidification.

3.2. Compression and energy absorption properties

The average compressive stress–strain curves (solid) with standard deviation band (dashed) of EHEA syntactic foam under quasi-static and dynamic conditions are shown in Fig. 3(a). The quasi-static and dynamic curves were averaged from five and four sets of data, respectively. The individual curves are shown in Fig. S2. At the strain rate of 10^{-3} s^{-1}, the compressive strength ($\sigma_c = \sigma_{1\%}$) and plateau stress (σ_p, average stress in the 20%–40% strain range) are 309.0 ± 13.0 MPa and 403.2 ± 26.2 MPa, respectively. The definitions of σ_c and σ_p follow the ISO 13314: 2011 standard [60]. The stress plateau ascends with moderate strain hardening in the front part of the curve, and then slightly downwards after a strain of 30%–35%. We define the densification strain (ε_d) of the sample to be 50% since the sample was severely damaged and almost failed at that time (see the inset macrograph). And the stress at ε_d is defined as densification strength (σ_d). The sample has a σ_d of 389.3 ± 40.5 MPa, slightly lower than σ_p, suggesting the whole plateau is flat and stable within a narrow stress range. At the strain rate of 2000 s^{-1}, the compressive strength (σ_c) and plateau stress (σ_p, average stress from 20% strain to the end) increase to 455.5 ± 28.4 MPa and 617.4 ± 73.3 MPa, respectively. The stress plateau is flat before 10% strain and keeps rising until the end, showing greater strain hardening.

To compare the mechanical properties of foam and matrix material, we present the representative compressive stress–strain curves of solid $AlCoCrFeNi_{2.1}$ matrix alloy under quasi-static and dynamic conditions in Fig. 3(b). The EHEA matrix shows high strength, and its yield strength ($\sigma_{0.2}$) is 670.2 ± 12.0 MPa and 959.5 ± 27.3 MPa for quasi-static and dynamic states, respectively. It is worth noting that the EHEA matrix fractured in a shear mode at a strain of 25–30%, exhibiting moderate ductility and a certain degree of brittleness. This feature is helpful to the formation of a flat stress platform for the MMSF.

Based on the stress–strain curves, we can further investigate the energy absorption properties. The energy absorption capacity (EAC) and energy absorption efficiency as a function of strains are plotted in Fig. 3(c) and (d). The energy absorption per unit volume,

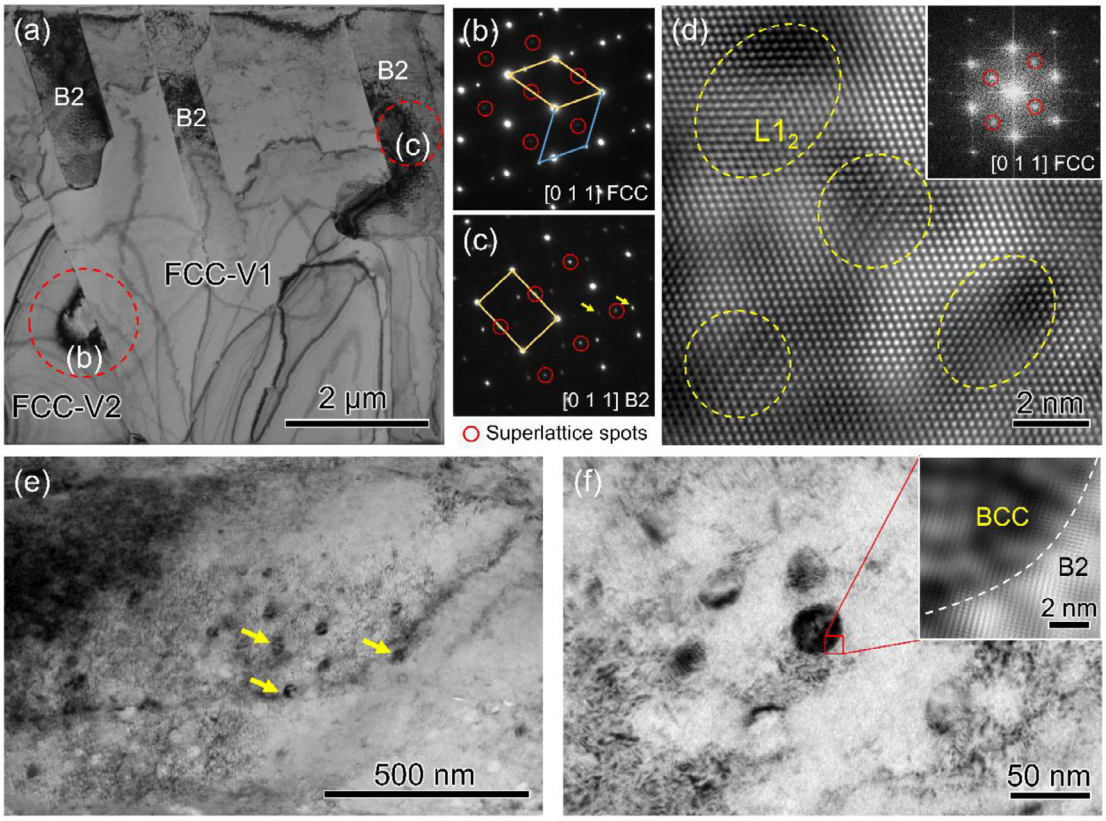

Fig. 2. The TEM observations of syntactic foam matrix. (a) The bright-field image of FCC/B2 lamellae and growth twin (V2) in FCC phase. (b) and (c) the SAED patterns of FCC phase and B2 phase, respectively. And the diffraction regions are marked by red circles in (a). (d) The HRTEM image showing the ordered $L1_2$ precipitates in FCC phase (marked by yellow circles), and the inset is the FFT pattern. (e) The bright-field image of B2 phase, and the BCC precipitates inside are indicated by yellow arrows. (f) The close-up view of BCC precipitates in B2 phase, the inset is the HRTEM image of the red frame area.

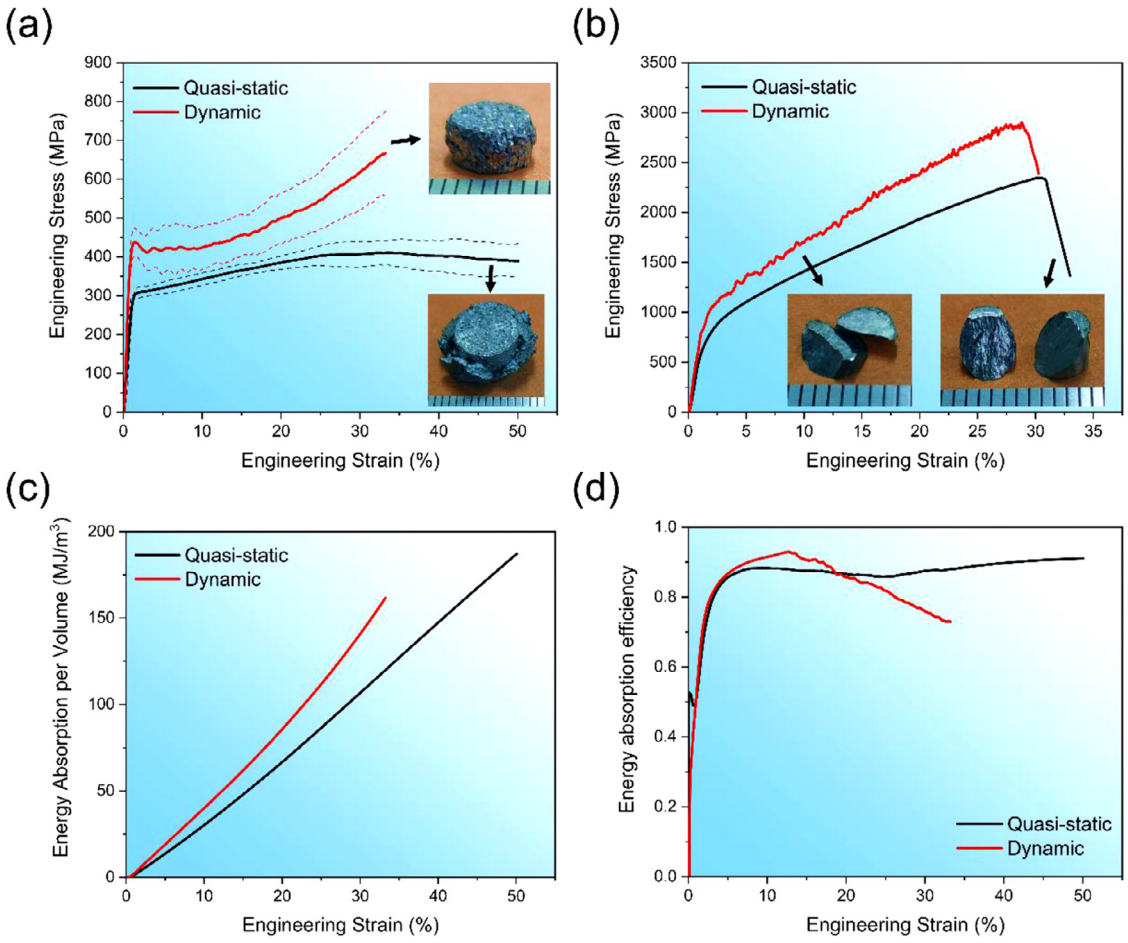

Fig. 3. Mechanical and energy absorption properties. (a) The average engineering stress–strain curves (solid) with standard deviation band (dashed) of syntactic foam under quasi-static and dynamic compression. (b) The representative stress–strain curves of solid $AlCoCrFeNi_{2.1}$ matrix under quasi-static and dynamic compression. (c) The energy absorption capacity and (d) the energy absorption efficiency of syntactic foam as a function of strain under quasi-static and dynamic compression.

W, is given by the area under the stress-strain curve and can be calculated by equation [65]:

$$W = \int_0^{\varepsilon} \sigma(\varepsilon')\mathrm{d}\varepsilon' \tag{1}$$

Under quasi-static compression up to a densification strain (ε_d) of 50%, W (50%) is 187.0 ± 10.1 MJ/m^3. Moreover, considering the density of the syntactic foam, the energy absorption per unit mass ($W_M(50\%) = W(50\%)/\rho_{SF}$) is 42.8 ± 2.1 kJ/kg. The EAC under dynamic compression is higher than that of quasi-static condition at the same strain due to the higher stress level of stress plateau. Whereas, due to the limitation of the experimental condition, the EAC up to the complete densification was not obtained.

Notably, it is incomprehensive to evaluate the energy absorption and cushioning performance based on the EAC alone because it only gives the amount of the absorbed energy [66,67]. Whereas the shape of the stress plateau, which is crucial in practical applications, cannot be reflected. As a protective material, the load transferred from syntactic foam to the internal objects during the impact should be less than the critical stress for the internal objects to be destroyed [68]. Under this constraint, to absorb more energy, the stress plateau of the syntactic foam needs to be as close as possible to this critical stress but cannot exceed it. Ideally, the stress–strain curve is rectangular in shape with the height equal to the critical stress. Accordingly, the energy absorption efficiency ($\eta(\varepsilon)$) is defined as the ratio of the energy absorbed by a real material to an ideal one [66,67,69,70]:

$$\eta(\varepsilon) = \frac{\int_0^{\varepsilon} \sigma(\varepsilon')\mathrm{d}\varepsilon'}{\sigma_{\max}(\varepsilon)\varepsilon} \tag{2}$$

where $\sigma_{\max}(\varepsilon)$ is the maximum stress on the stress–strain curve up to the strain ε. The closer the $\eta(\varepsilon)$ to unity, the more ideal the energy absorption behavior and the flatter the stress plateau of the material. The EHEA syntactic foam has an $\eta(\varepsilon)$ of 0.86–0.91 under quasi-static compression in the strain range of 5% to 50%, which is reflected on its flat stress plateau. Under dynamic compression, $\eta(\varepsilon)$ has a peak value of 0.93 at a strain of ~10%. Although it gradually decreases due to the ascending stress plateau, it still has a value over 0.75. The mechanical and energy ab-

Table 2
Mechanical properties of EHEA syntactic foams.

	Compressive strength, σ_c (MPa)	Plateau stress, σ_p (MPa)	Densification strength, σ_d (MPa)	Densification strain, ε_d (%)	Energy absorption per volume, W (50%)(MJ/m^3)	Energy absorption per mass, W_M (50%) (kJ/kg)	Energy absorption Efficiency, $\eta(\varepsilon)$ (ε > 5%)
Quasi-static	309.0 ± 13.0	403.2 ± 26.2	389.3 ± 40.5	50.0 ± 0.0	187.0 ± 10.1	42.8 ± 2.1	0.86–0.91
Dynamic	455.5 ± 28.4	617.4 ± 73.3	–	–	–	–	0.75–0.93

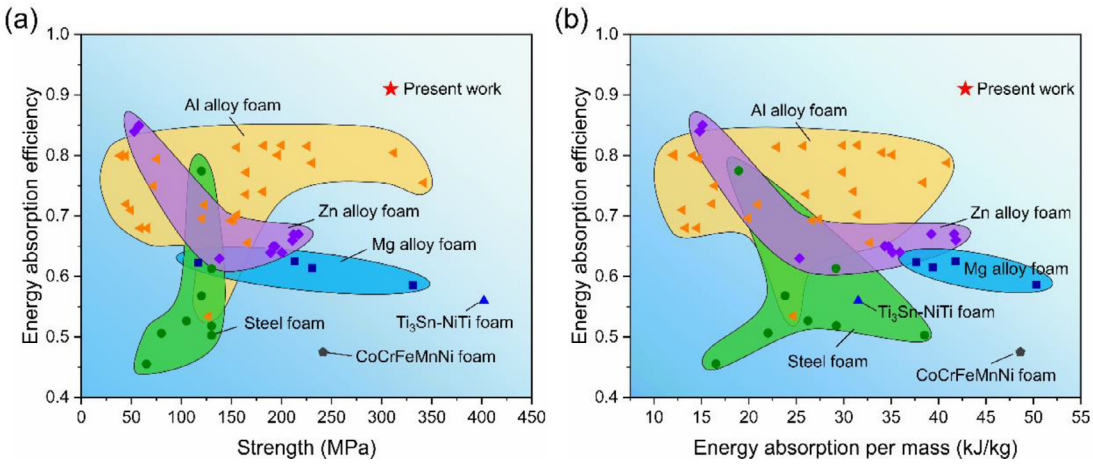

Fig. 4. Summary of the strength and energy absorption properties of various MMSFs under quasi-static compression. (a) Energy absorption efficiency versus strength (compressive or peak strength on their definition). (b) Energy absorption efficiency versus energy absorption per mass. The data on energy absorption efficiency are taken from the value at the densification strain. Some energy absorption efficiency data not presented in the literature were measured from the stress–strain curves. References: Al alloy foams [12,23,65,71,72], Zn alloy foams [70,73], Mg alloy foams [18,71], steel foams [14,24], Ti_3Sn-NiTi foam [19], CoCrFeMnNi foam [25].

sorption properties of EHEA syntactic foam are listed in Table 2. Fig. 4 summarizes the strength, energy absorption capacity and efficiency of various MMSFs under quasi-static compression. We directly compare these properties with those of conventional MMSFs, thereby demonstrating the singular combination of high strength and energy absorption performance of $AlCoCrFeNi_{2.1}$ syntactic foam.

3.3. Deformation mechanism of quasi-static compression

3.3.1. Macroscopic deformation behavior

Fig. 5(a1–e1) are CT reconstructed 3D images of EHEA syntactic foams interrupted at different deformation strains, while Fig. 5(a2–e2) are the corresponding section slices. At the early stage of deformation (10% strain, Fig. 5(a1) and (a2)), the weak points in the foam broke, connected, and formed a deformed layer. At a strain of 20% (Fig. 5(b1) and (b2)), the stress increases with the rupture and compaction of the weak pores. From the corners of the sample, cracks expanded through a set of aligned pores along the direction of the maximum shear stress. Owing to the ductility of the matrix and the misaligned pores, cracks stopped in the middle rather than penetrating through the sample. As the deformation further increased (30% strain, Fig. 5(c1) and (c2)), shear cracks appeared at all four corners, and the middle part of the specimen was also fractured under compression. At this time, the stress plateau reached the top (Fig. 3(a)). At a higher strain of 40% (Fig. 5(d1) and (d2)), the middle part of the sample was compacted, while the periphery was continuously extruded sideways, causing large cracks. As the load-bearing area decreases, the stress plateau begins to fall (Fig. 3(a)). Finally, when the strain reached 50% (Fig. 5(e1) and (e2)), the pores in the middle part were compacted, and the peripheral part was also severely squeezed out, accompanied by the fragments falling off the matrix. As a result, the sample was nearly densified and could not absorb energy effectively. The SEM images of samples interrupted at different deformation strains are shown in Fig. S3, which can provide more details.

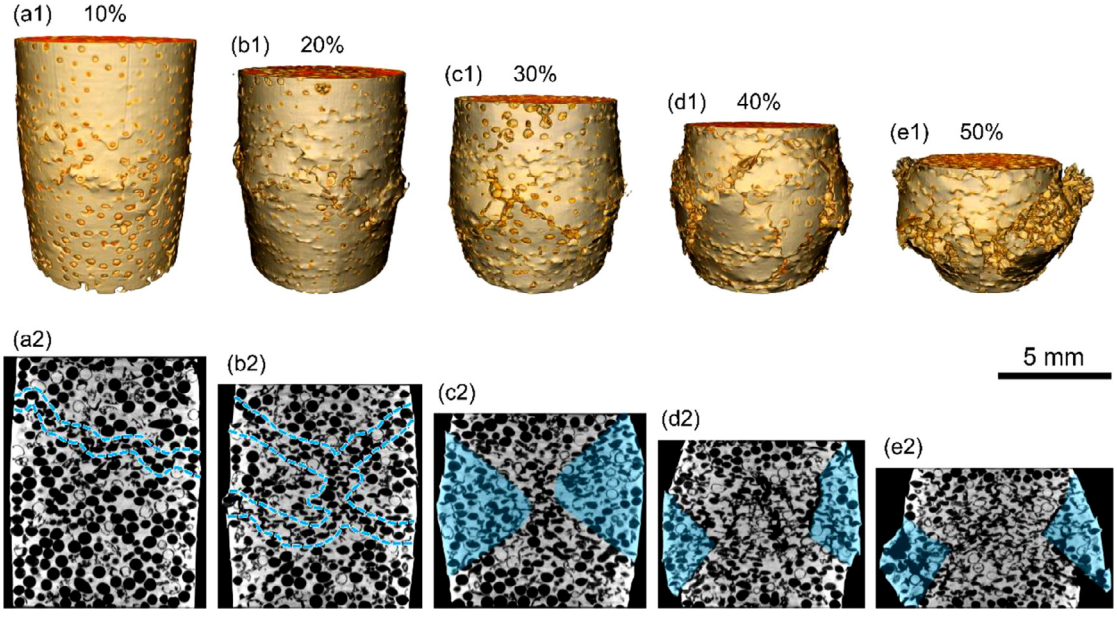

Fig. 5. Computed tomography characterizations of deformed syntactic foam samples interrupted at strains of 10%–50%. (a1–e1) The reconstructed 3D images. (a2–e2) The corresponding section slices.

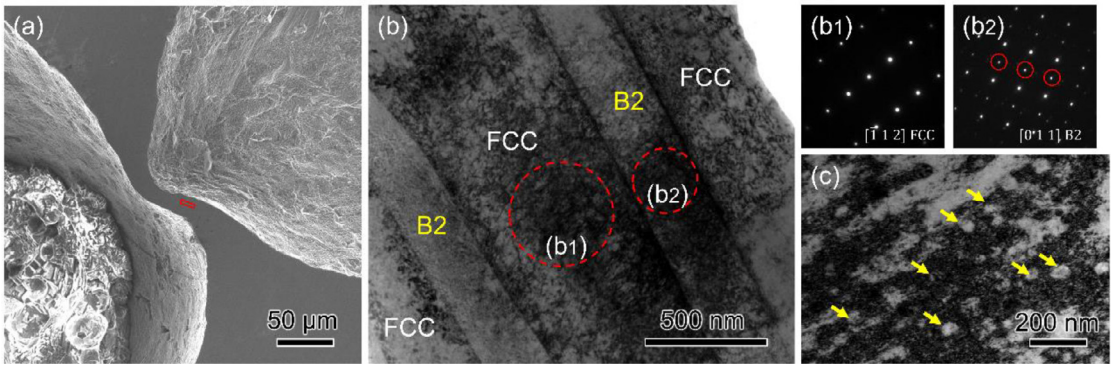

Fig. 6. The characterizations of a plastically bent strut. (a) The secondary electron morphology. The red frame indicates the position of TEM sample. (b) The TEM bright-field image showing the FCC/B2 lamellar microstructure, and the corresponding SAED patterns are shown in (b1) FCC phase and (b2) B2 phase, diffraction regions are marked by red circles. (c) The bright-field image of B2 phase shows the interaction between dislocations and Cr-rich BCC precipitate particles (indicated by yellow arrows).

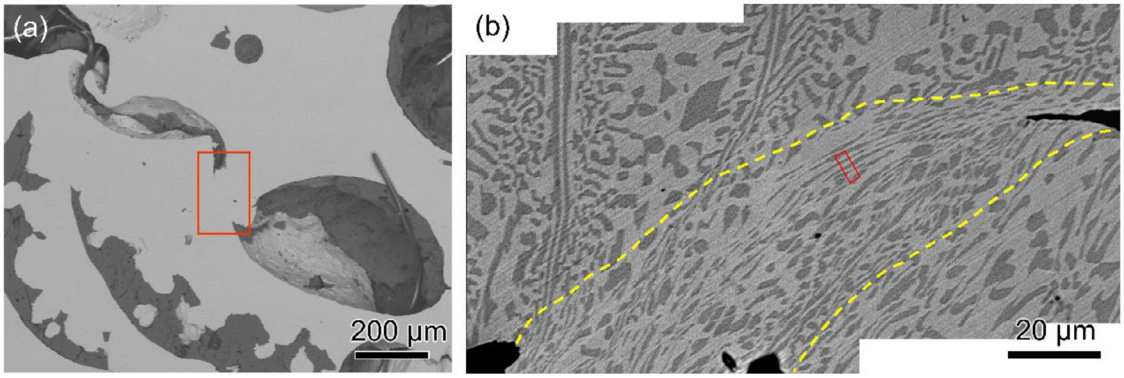

Fig. 7. The SEM images of shear fractured struts. (a) The secondary electron morphology of shear fractured pores. (b) The high magnification BSE image of the red frame area in (a) showing the shear localization in the strut (outlined by yellow dashed lines). The darker phase is B2, and the lighter phase is FCC. The red rectangle marks the position for FIB milling to prepare TEM foil.

3.3.2. Microstructure characterization of deformed struts

Since the main deformation modes of the matrix are the bending and shearing of struts, we carried out detailed characterizations to explain the deformation micro-mechanisms. Fig. 6 shows the morphology and microstructure of a plastically bent strut. As shown in Fig. 6(b), there is a high density of dislocations in FCC/B2 lamellae, suggesting both phases experienced extensive plastic deformation. However, the deformation is inhomogeneous due to the differences in hardness and modulus of the two phases [74]. The soft FCC phase affords more plastic deformation than the hard B2 phase and creates strain gradients nearby the FCC/B2 interfaces. To accommodate the inhomogeneous deformation, large amounts of geometrically necessary dislocations (GNDs) [75–78] were generated, and the darker contrast of the phase interfaces implied their existence. The GNDs can hinder the motion of other mobile dislocations and hence contribute to the strain hardening of the matrix. In addition, the BCC precipitates in B2 phase acted as obstacles to the dislocation movement (Fig. 6(c)) and resulted in precipitation strengthening [50]. However, the $L1_2$-ordered precipitates in the FCC phase were not found, which can be confirmed by the absence of superlattice patterns (Fig. 6(b1)). This indicates the disordering of $L1_2$ phases into FCC during plastic deformation [52,79]. After having been passed by several dislocations, the ordered structure of $L1_2$ and antiphase boundaries were destroyed, and the strengthening by ordered precipitates was also exhausted. This is one reason why the hardening of the material decreases in the later stage of deformation.

The morphology of shear fractured struts is shown in Fig. 7(a). The magnified backscattered electron (BSE) image (red frame region in Fig. 7(a)) is shown in Fig. 7(b). It is evident that the region between two yellow dashed lines experienced severe shear deformation, and cracks had nucleated at both ends. In addition, the original irregular B2 phases in this region were elongated to strips, and the lamellar B2 phases nearby also bent along the shear direction. To study the microstructural features of this shear localized zone, we prepared TEM foil samples by FIB milling technique from the red frame area in Fig. 7(b).

The montage in Fig. 8(a) shows the TEM bright-field image of an elongated B2 phase and surrounding FCC phases in a shear localized zone. The microstructure shows complex morphology with fine substructures in both phases. In the B2 phase, it can be seen that the dislocations have rearranged into cell structures and evolved into several subgrains (Fig. 8(c)). The corresponding reflection spots shown in Fig. 8(b) are stretched, suggesting the formation of the small-angle boundaries. Compared with the B2 phase, the FCC phase underwent severer plastic deformation. As shown in Fig. 8(a), FCC grains split into fine equiaxed subgrains and elongated lath subgrains and could be proved by the SAED pattern (Fig. 8(d)), which shows incomplete rings. Fig. 8(e) shows a closer examination of these fine subgrains. The interior subgrains were separated by dislocation tangles, and no sharp grain boundaries were found. Considering that the sample deformed under quasi-static loading, the temperature in the shear localized zone should be lower than the recrystallization temperature. Therefore, the development of these fine substructures may be attributed to dynamic recovery. Fig. 8(f) shows the SAED pattern from the elongated subgrains area, two sets of patterns can be seen. The pattern along [0 0 1] zone axis is stretched (marked by green lines), and the pattern along [0 1 1] zone axis shows the reflection pattern of twins, suggesting that this area is composed of lath subgrains and

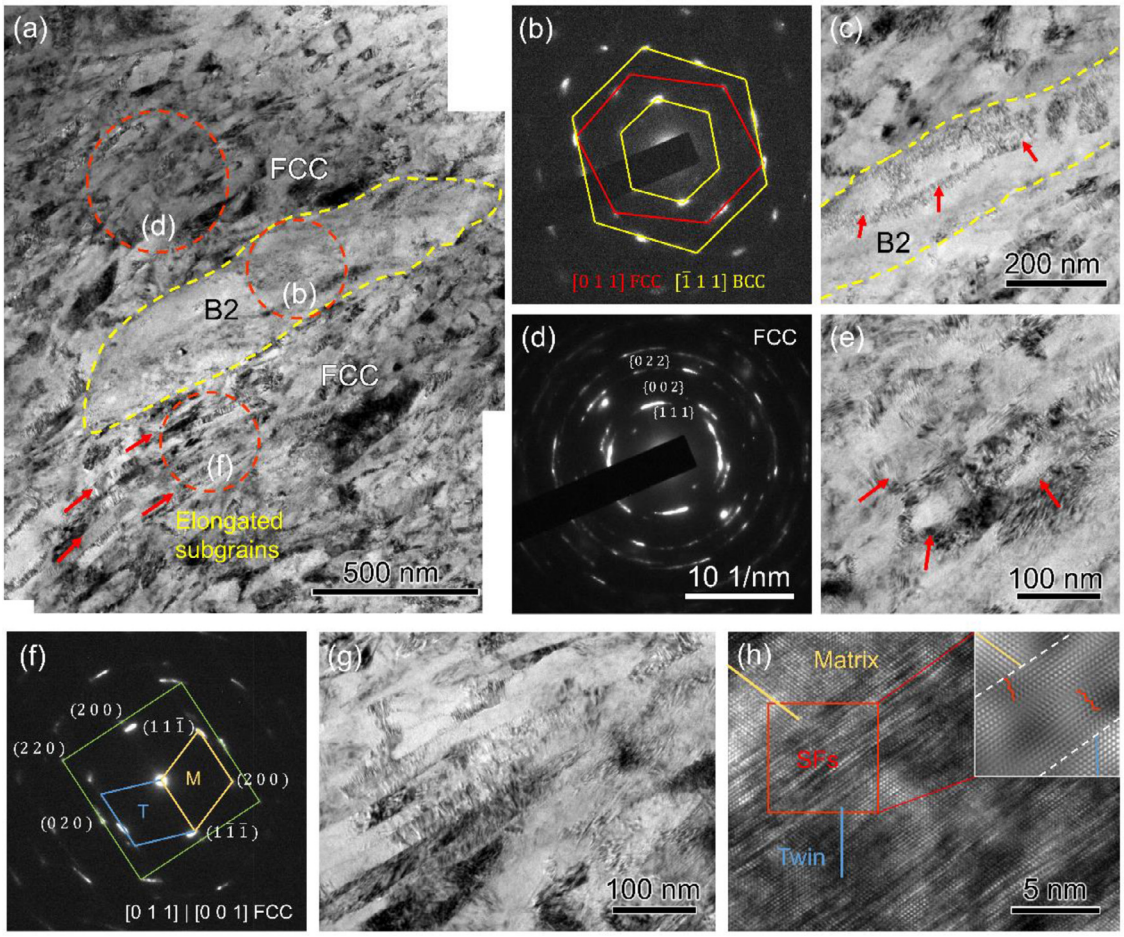

Fig. 8. The TEM characterizations of the shear localized zone marked by the red frame in Fig. 7(b). (a) The bright-field image of an elongated B2 phase and surrounding FCC phases. Red circles indicate the diffraction regions of (b), (d), and (f). (b) The SAED pattern of B2 phase (the additional diffraction spots marked by red lines belong to the adjacent FCC phase). (c) The subgrains in B2 phase (indicated by red arrows). (d) The SAED pattern of fine equiaxed subgrains in FCC phase. (e) The close-up view of equiaxed subgrains (indicated by red arrows) within FCC phase. (f) The SAED pattern of elongated subgrains and deformation twins in FCC phase. (g) The bright-field morphology of elongated subgrains and twins. (h) The HRTEM image shows the twin and stacking faults (SFs). Inset is the zoom-in image of the red frame area after Fourier transform filtering.

deformation twins. More detailed images are shown in Fig. 8(g) and (h). The twins with straight boundaries and the elongated laths with high-density dislocations are visible. And the HRTEM image of the deformation twin shows multiple stacking faults between the matrix and twin, indicating that the twin boundary is severely deformed. These fine subgrains and elongated subgrains are typical characteristics in shear localization [80–82], suggesting the material softening under shear deformation.

3.4. Deformation mechanism of dynamic compression

3.4.1. Macroscopic deformation behavior

Fig. 9 shows the SEM images of MMSF samples interrupted at different strains under dynamic compression. Compared with the quasi-static condition, the MMSF sample deformed more severely and abruptly under dynamic compression, resulting in a significant temperature rise in the material. This high temperature promotes thermal softening and makes materials more susceptible to shear localization [83] and subsequent failure. Therefore, the stress–strain curve is flat with less strain hardening before a strain of 10% (Fig. 3(a)). Nevertheless, this abrupt deformation rapidly exhausts the plastically bent struts and leads to densification at the early stage. As shown in Fig. 9(c) and (d), after a strain of 20%, a tortuous crack penetrated the matrix approximately along the direction of the maximum shear stress, and there were two secondary cracks intersected the main crack. On both sides of the main crack, the pores were shear fractured and compacted together, so that the MMSF can withstand greater loads, which made the stress plateau start to rise (Fig. 3(a)).

Closer examinations of the deformed samples are shown in Fig. 9(e–h). Fig. 9(e and f) shows the close-up view of a shear-fractured strut in the deformed layer (red frame area in Fig. 9(b)). Obviously, the matrix experienced a large amount of plastic deformation indicated by the plastically bent lamellar B2 phase (as shown in the inset). Fig. 9(g) shows the morphology of a collapsed pore and severely deformed struts. These struts were bent or fractured, and a shear band can be found in one strut. It is clear that irregular B2 islands are deformed and stretched within the shear band, and the crack nucleated at the end of the shear band and propagated through it (Fig. 9(f)). This observation implies that the irregular B2 islands could induce the formation of shear bands and subsequent nucleation of cracks. Other representative deformation images are shown in Fig. S4, and the TEM sampling locations are marked by red rectangles in Fig. S4(b) and (d).

3.4.2. Microstructure characterization of deformed struts

Fig. 10 shows the microstructure of a deformed strut. Similar to quasi-static compression, there is a high density of dislocations in

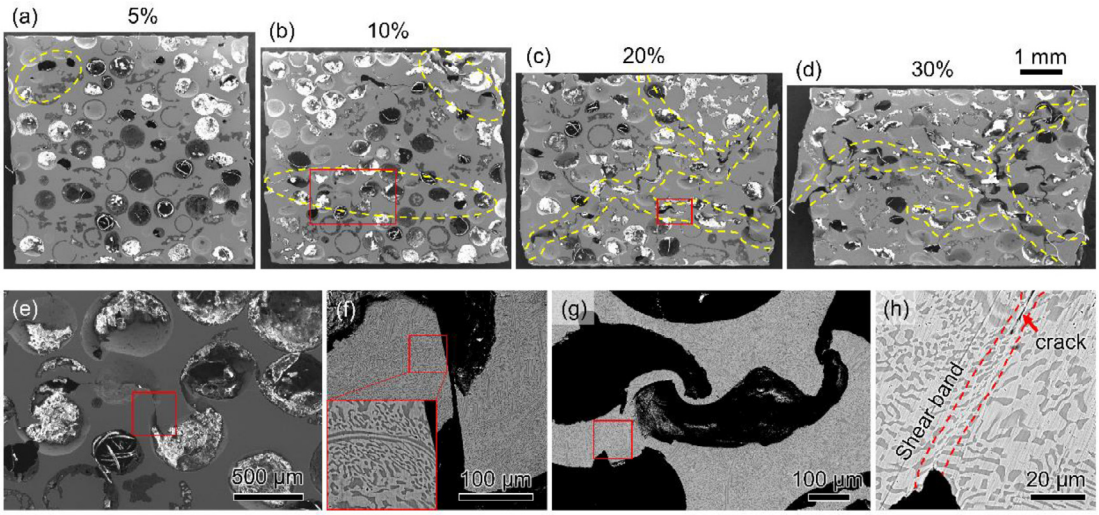

Fig. 9. The SEM images of deformed syntactic foams under dynamic compression. (a–d) The morphology of deformed samples interrupted at strains of 5%–30%. Deformed regions or cracks are outlined by yellow dashed lines. (e) The close-up view of the red frame area in (b). (f) The BSE image of the red frame area in (e). (g) The close-up view of the red frame area in (c). (h) The zoom-in image of the red frame area in (g).

both phases (Fig. 10(a)). In the FCC lamellae, dislocations formed cell structures (pointed by red arrows), and the corresponding reflection spots (Fig. 10(a1)) are stretched and split, which suggests that the dislocation cells have evolved into subgrains. Unlike quasi-static compression, substantial nano-spaced stacking faults can be discerned in the FCC phase (Fig. 10(b)). These stacking faults (marked by red and yellow arrows) were activated on two {1 1 1} slip systems and intersected with each other. The HRTEM image (Fig. 10(c)) shows the enlarged morphology of extensive stacking fault intersections and Lomer-Cottrell (L-C) locks (indicated by red arrows). And the corresponding FFT patterns (Fig. 10(c1)) exhibit two crossing diffraction fringes (red arrows), suggesting the presence of stacking faults on two {1 1 1} planes. The immobile L-C locks are formed by the interaction of two leading Shockley partials from two dissociated dislocations. They can act as strong barriers to the movement of other mobile dislocations, which strengthen the FCC phase and promote the dislocation density to accommodate plastic deformation [84–86]. The strengthening effect and additional source of strain hardening produced by intersected stacking faults and L-C locks are the important reasons for the increase of strength and strain hardening of the syntactic foam under dynamic compression.

The montage in Fig. 11(a) shows the microstructure of a shear band marked in Fig. S4(d). From the center to the boundary, the microstructure in each phase changed with decreasing shear deformation. For the B2 phase on the left of the shear band center, a high density of dislocations separated the grain into several elongated subgrains. The magnified image is shown in Fig. 11(b). It can be seen that dislocations aligned on the subgrain boundaries, and the slight elongation of SAED patterns along the circumferential direction reveals the presence of small-angle boundaries in the substructure. This indicates that the hard B2 phase deformed severely under shear stress. While the adjacent FCC phase experienced severer plastic deformation due to the lower strength and hardness. As shown in Fig. 11(c), grains within the FCC phase have split into several elongated lath subgrains and fine equiaxed recrystallized grains. The zoom-in image of these subgrains is shown in Fig. 11(d). Among equiaxed fine subgrains, some rectangular subgrains can be observed. Compared to those elongated subgrains, their aspect ratios (length/width) are reduced and close to those of equiaxed recrystallized grains, which suggests the transition from elongated subgrains to fine recrystallized grains. This transition could be delineated by a splitting and breakdown mechanism [80,87]. The large shear stress along the shear direction results in the splitting of grains and forms elongated subgrains. While the conjugated shear stresses break down the elongated subgrains into pieces with a reduced aspect ratio. This linkage of the elongated and equiaxed subgrains indicates that the grain refinement in FCC did not evolve from typical nucleation and growth of recrystallization but a deformation-induced mechanism, namely the rotational dynamic recrystallization [83,87].

As it moves away from the shear band center, the deformation decreases. The B2 phase on the right of the shear band center also has large amounts of dislocations but exhibits no subgrains since the diffraction spots do not reveal the separation of reflections. Next to this B2 lamellae, the FCC phase exhibits severe plastic deformation but less than that on the center. The corresponding SAED pattern is stretched and nearly forms a ring suggesting that grains have split into multiple fine subgrains. As shown in Fig. 11(e), subgrains with high-density dislocations are visible, and the substructure boundaries are blurred, sharp boundaries with high misorientation angle were not formed. In addition, a closer examination (Fig. 11(f)) shows the existence of deformation twins. The twin relationship can be confirmed by the HRTEM image (Fig. 11(g)) and FFT pattern (inset). There are also several stacking faults between the twins and the matrix. These twins and stacking faults may occur in the early stage of deformation and diminish with the increase of deformation by dynamic recrystallization.

4. Discussion

4.1. The origin of high compressive strength

Compared with other MMSFs (Fig. 4), the present $AlCoCrFeNi_{2.1}$ EHEA syntactic foam exhibits an excellent combination of high strength and energy absorption performance, which mainly originate from the unique FCC/B2 dual-phase eutectic microstructure of the $AlCoCrFeNi_{2.1}$ alloy matrix.

A variety of strengthening mechanisms of the $AlCoCrFeNi_{2.1}$ matrix ensure the high strength of the syntactic foam. Firstly, the hard and strong B2 phase can act as reinforcement and bear large amounts of load transferred from the soft FCC phase, similar to the rigid particles in the metal matrix composites [88]. Secondly,

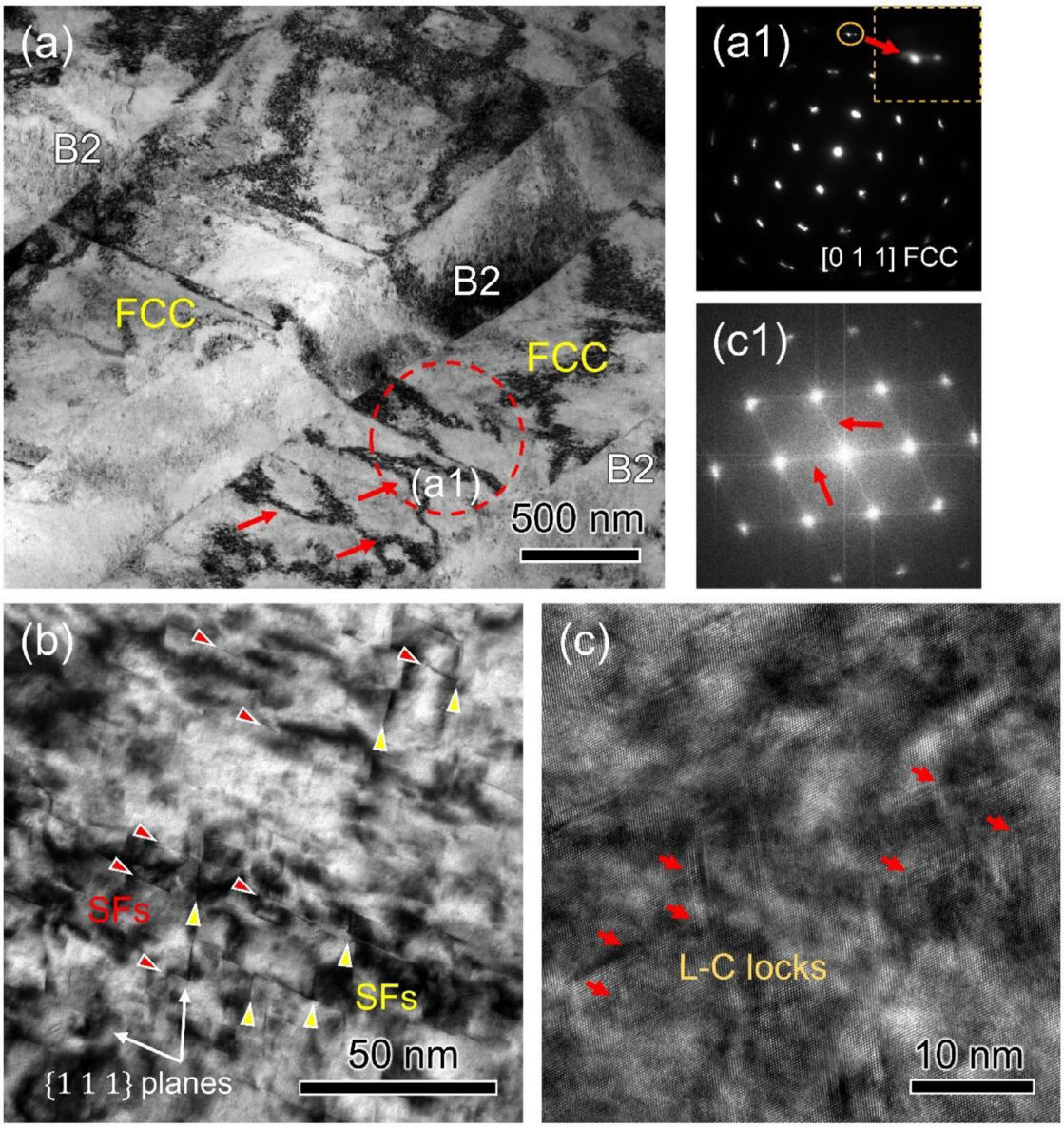

Fig. 10. The TEM characterizations of a deformed strut (the rectangular area in Fig. S4(b)). (a) The bright-field image of FCC/B2 lamellae. Red arrows indicate the dislocation cells. (a1) The SAED pattern of the region marked with circle in (a). The inset shows the separation of diffraction spots. (b) The magnified bright-field image of FCC phase shows intersected stacking faults (SFs) on two {1 1 1} slip planes. (c) The HRTEM image of intersected stacking faults and L-C locks, and the corresponding FFT patterns are shown in (c1).

the constraint of hard B2 lamellae can strengthen the soft FCC lamellae [53,54]. During the deformation, the soft FCC lamellae will deform plastically first. However, they cannot deform freely owing to the constraint of the surrounding B2 phase. The deformation incompatibility leads to strain gradients at the interface, and the GNDs are generated and stored in the FCC lamellae consequently (Fig. 6(b)). This process produces long-range back stress, making it difficult for dislocations to slip in the FCC lamellae until the B2 phase yields [54]. Thus, the strength of FCC lamellae is elevated. Thirdly, there exist a large number of various interfaces in the matrix, such as grain boundaries, phase interfaces, and twin boundaries (Figs. 1 and 2). These interfaces are strong barriers to the movement of dislocations and can strengthen the matrix by reducing the dislocation mean free path [54]. In addition, the $L1_2$ and Cr-rich BCC precipitate particles in FCC and B2 phases also contribute to the strength by precipitation strengthening [50,54].

4.2. Deformation mechanisms and energy absorption performance

The energy absorption performance depends on the shape of the stress plateau and is closely related to the deformation mechanisms [16,89,90]. According to the results of CT and SEM observations (Figs. 5 and S3), the MMSF deformed in a diffuse mode [9,15] rather than fractured abruptly, which means that the damages of the sample are dispersive and progressive. At the early deformation stage, some weak struts start to bend plastically first and then fracture as the deformation increases (Fig. S3(a)). After that, the additional load is partitioned to the adjacent struts, causing them to bend and fracture subsequently. As this process continues, the deformation expands to several layers of pores in the middle of the matrix (Fig. 5(a1, a2)). During this period, the strain hardening of the plastically bent struts was slightly greater than the softening effect caused by the fracture. Therefore, the stress plateau showed an upward trend. However, if the MMSF always

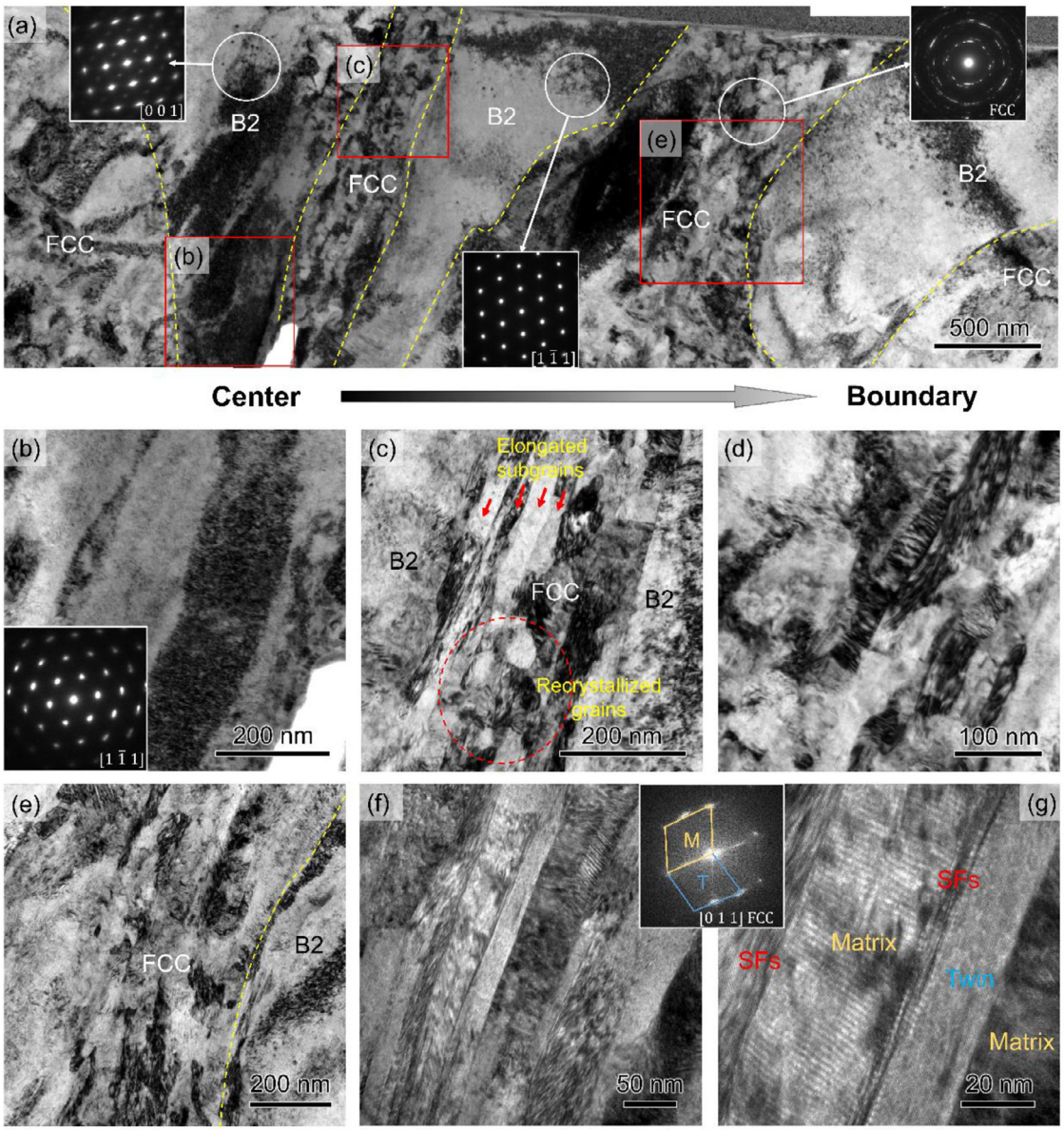

Fig. 11. The TEM characterizations of a shear band marked by a red frame in Fig. S4 (d). (a) The montage of the shear band from the center to its boundary. (b) The bright-field image of subgrains inside the B2 phase, inset is the SAED patterns. (c) The bright-field image of the FCC phase near the shear band center. (d) The higher magnification morphology of the subgrains in FCC phase. (e) The bright-field image of the FCC phase away from the shear band center. (f) The zoom-in image of (e), showing deformation twins in FCC phase. (g) The HRTEM image of deformation twins and stacking faults. Inset is the corresponding FFT pattern.

shows a greater strain-hardening effect during the deformation, a monotonously rising stress plateau will appear like some ductile MMSFs [14,25], which will reduce the energy absorption efficiency. For $AlCoCrFeNi_{2.1}$ syntactic foam, shear failure occurs at the corners of the sample at a strain of 20–30% and increases the softening effect (Fig. 5(c1, c2)). Meanwhile, the proportion of plastically bent struts decreases with the development of deformation so that the strain-hardening effect becomes weak. Therefore, as the softening effect exceeds the hardening effect, the stress plateau begins to drop slightly. During the deformation process, the synergistic effects of multiple deformation mechanisms (plastic bending, shear localization, and microcracks) maintain the approximate balance of softening and hardening, thus leading to this long and flat stress plateau and avoiding continuous rising stress or large stress oscillations.

The microstructural characterizations of deformed struts explain the underlying mechanisms of hardening and softening from the micro-scale. Due to the differences in mechanical properties between the constituent phases, the deformation is heterogeneous. Soft FCC phases carry a larger strain than hard B2 phases, and strain gradients are created nearby the FCC/B2 interfaces. Accordingly, the GNDs were generated and stored near the phase interfaces to accommodate the heterogeneous deformation between the two phases (Fig. 6(b)). They acted as barriers to other mobile dislocations, causing considerable back stress hardening [53,54,75]. As the deformation increases, the strain gradients between the two phases also make the matrix more susceptible to shear localization and cause softening effects. Previous research in particle-reinforced metal matrix composites (MMCp) shows that high strain gradient induced by small rigid particles provides a strong driving force for the formation of shear bands [91,92]. In $AlCoCrFeNi_{2.1}$ matrix, the irregular B2 islands play the same role as the rigid particles in MMCp on the formation of shear localization (Figs. 7 and 9(h)). However, due to the buffer of the ductile FCC phase, these shear

localizations did not rapidly evolve into cracks and caused catastrophic failure. As shown in Figs. 8 and 11, the FCC grains split into elongated subgrains and dynamically recovered/recrystallized into fine equiaxed subgrains. And some deformation twins and stacking faults were also formed to accommodate large deformation and provide strain hardening. So that the nucleation and propagation of cracks along the path of the shear band are suppressed. In addition, it is worth noting that the transition from ordered $L1_2$ precipitates to disordered FCC during the deformation (Fig. 6(b1)). The ordered $L1_2$ precipitates that initially existed in the FCC phase could provide precipitation and order strengthening at the early deformation stage. As the deformation proceeds, the ordered $L1_2$ structure was destroyed, and the corresponding strengthening was exhausted, leading to the softening of the material in the later deformation stage. However, the disordered FCC phase is more ductile than the ordered $L1_2$ phase [79,93]. Therefore, the disordering is helpful to the resistance to crack nucleation and propagation.

5. Conclusions

In this study, a new metal matrix syntactic foam fabricated with $AlCoCrFeNi_{2.1}$ eutectic high entropy alloy and alumina cenospheres was developed by gas pressure infiltration method and exhibited an excellent combination of high strength and energy absorption performance under quasi-static and dynamic compression. We investigated the macroscopic deformation behavior and microstructure evolution to reveal the underlying mechanisms. The main conclusions are summarized as follows:

(1) The syntactic foam has a high compressive strength of 309.0 ± 13.0 MPa and 455.5 ± 28.4 MPa under quasi-static and dynamic compression, respectively. Meanwhile, it has an energy absorption capacity of 187.0 ± 10.1 MJ/m^3 at 50% strain and keeps an energy absorption efficiency of 0.86–0.91 during the stress plateau under quasi-static compression.
(2) The FCC/B2 lamellar eutectic microstructure of the $AlCoCrFeNi_{2.1}$ matrix plays an important role in the excellent performance of the syntactic foam.
(3) The syntactic foam has a variety of deformation mechanisms during the failure process, including plastic bending, shear localization, and microcracks. Their cooperation maintains the approximate balance of hardening and softening so that the energy absorption platform is long and flat.
(4) The strain gradients created by the heterogeneity between FCC/B2 phases during deformation have twofold effects: providing back stress strengthening and inducing shear localization and microcracks as the deformation proceeds.
(5) Under dynamic compression, the sample deformed severer and more abruptly, leading to densification at the early stage. In addition, massive intersected stacking faults and Lomer-Cottrell locks formed in the FCC phase provide additional strain hardening. Therefore, the stress plateau shows more significant strain hardening, reducing the energy absorption efficiency.

Declaration of Competing Interest

The authors declare that they have no known competing financial interests or personal relationships that could have appeared to influence the work reported in this paper.

Acknowledgements

This research was supported by the NSFC Basic Science Center Program for “Multiscale Problems in Nonlinear Mechanics” (No. 11988102), the NSFC (Nos. 11790292, 11972346 and 11672316), Ye Qisun Science Foundation of NSFC (No. U2141204), the Key Research Program of the Chinese Academy of Sciences (No. ZDRW-CN-2021-2-3), and the Strategic Priority Research Program of the Chinese Academy of Sciences (Nos. XDB22040302 and XDB22040303).

Supplementary materials

Supplementary material associated with this article can be found, in the online version, at doi:10.1016/j.jmst.2022.12.009.

References

[1] L.J. Gibson, M.F. Ashby, Cellular Solids: Structure and Properties, 2nd ed., Cambridge University Press, Cambridge, 1997.
[2] M.F. Ashby, A. Evans, N.A. Fleck, L.J. Gibson, J.W. Hutchinson, H.N.G. Wadley, Mater. Des. 23 (1) (2002) 119.
[3] L.O. Afolabi, Z.M. Ariff, S.F.S. Hashim, T. Alomayri, S. Mahzan, K.-A. Kamarudin, I.D. Muhammad, J. Mater. Res. Technol. 9 (5) (2020) 10698–10718.
[4] Y. Zhang, G. Tan, D. Jiao, J. Zhang, S. Wang, F. Liu, Z. Liu, L. Zhuo, Z. Zhang, S. Deville, R.O. Ritchie, J. Mater. Sci. Technol. 45 (2020) 187–197.
[5] J.W. Chua, X. Li, T. Li, B.W. Chua, X. Yu, W. Zhai, J. Mater. Sci. Technol. 108 (2022) 196–207.
[6] T. Wan, Y. Liu, C. Zhou, X. Chen, Y. Li, Fabrication, J. Mater. Sci. Technol. 62 (2021) 11–24.
[7] Li Xiang, Yan Ziming, Liu Zhanli, Z. Zhuo, Adv. Mech. 51 (1) (2021) 82–105.
[8] J. Marx, A. Rabiei, Adv. Eng. Mater. 19 (11) (2017) 1600776.
[9] I.N. Orbulov, A. Szlancsik, Adv. Eng. Mater. 20 (5) (2018) 1700980.
[10] I.N. Orbulov, Metal Matrix Composite Syntactic Foams for Light-Weight Structural Materials, Reference Module in Materials Science and Materials Engineering, Elsevier, 2021.
[11] Y. Lin, Q. Zhang, J. Chang, H. Wang, X. Feng, J. Wang, Mater. Sci. Eng. A 766 (2019) 138338.
[12] J.A. Santa Maria, B.F. Schultz, J.B. Ferguson, P.K. Rohatgi, Mater. Sci. Eng. A 582 (2013) 415–422.
[13] I.N. Orbulov, J. Ginsztler, Compos. Pt. A-Appl. Sci. Manuf. 43 (4) (2012) 553–561.
[14] G. Castro, S.R. Nutt, Mater. Sci. Eng. A 553 (2012) 89–95.
[15] B. Katona, A. Szlancsik, T. Tábi, I.N. Orbulov, Mater. Sci. Eng. A 739 (2019) 140–148.
[16] Y.H. Song, M. Tane, H. Nakajima, Acta Mater. 60 (3) (2012) 1149–1160.
[17] D.K. Balch, J.G. O'Dwyer, G.R. Davis, C.M. Cady, G.T. Gray, D.C. Dunand, Mater. Sci. Eng. A 391 (1) (2005) 408–417.
[18] D.B. Newsome, B.F. Schultz, J.B. Ferguson, P.K. Rohatgi, Materials (Basel) 8 (9) (2015) 6085–6095.
[19] C. Xie, H. Li, B. Yuan, Y. Gao, Z. Luo, M. Zhu, ACS Appl. Mater. Interfaces 11 (31) (2019) 28043–28051.
[20] G.H. Wu, Z.Y. Dou, D.L. Sun, L.T. Jiang, B.S. Ding, B.F. He, Scr. Mater. 56 (3) (2007) 221–224.
[21] Y. Lin, Q. Zhang, F. Zhang, J. Chang, G. Wu, Mater. Sci. Eng. A 696 (2017) 236–247.
[22] M. Taherishargh, I.V. Belova, G.E. Murch, T. Fiedler, Mater. Sci. Eng. A 635 (2015) 102–108.
[23] M. Su, H. Wang, H. Hao, T. Fiedler, J. Alloy. Compd. 821 (2020) 153233.
[24] G. Castro, S.R. Nutt, Mater. Sci. Eng. A 535 (2012) 274–280.
[25] J. Meng, T.-W. Liu, H.-Y. Wang, L.-H. Dai, Compos. Pt. B-Eng. 207 (2021) 108563.
[26] J.-W. Yeh, S.-K. Chen, S.-J. Lin, J.-Y. Gan, T.-S. Chin, T.-T. Shun, C.-H. Tsau, S.-Y. Chang, Adv. Eng. Mater. 6 (5) (2004) 299–303.
[27] B. Cantor, I.T.H. Chang, P. Knight, A.J.B. Vincent, Mater. Sci. Eng. A 375-377 (2004) 213–218.
[28] E.P. George, D. Raabe, R.O. Ritchie, Nat. Rev. Mater. 4 (8) (2019) 515–534.
[29] Q. Pan, L. Zhang, R. Feng, Q. Lu, K. An, A.C. Chuang, J.D. Poplawsky, P.K. Liaw, L. Lu, Science 374 (6570) (2021) 984–989.
[30] Y. Bu, Y. Wu, Z. Lei, X. Yuan, H. Wu, X. Feng, J. Liu, J. Ding, Y. Lu, H. Wang, Z. Lu, W. Yang, Mater. Today 46 (2021) 28–34.
[31] L. Li, R.D. Kamachali, Z. Li, Z. Zhang, Phys. Rev. Mater. 4 (5) (2020) 053603.
[32] Y. Fu, J. Li, H. Luo, C. Du, X. Li, J. Mater. Sci. Technol. 80 (2021) 217–233.
[33] B. Yeqiang, W. Hongtao, Adv. Mech. 51 (4) (2021) 915–919.
[34] W. Li, D. Xie, D. Li, Y. Zhang, Y. Gao, P.K. Liaw, Prog. Mater. Sci. 118 (2021) 100777.
[35] Z. Li, S. Zhao, R.O. Ritchie, M.A. Meyers, Prog. Mater. Sci. 102 (2019) 296–345.
[36] X.-F. Liu, Z.-L. Tian, X.-F. Zhang, H.-H. Chen, T.-W. Liu, Y. Chen, Y.-J. Wang, L.-H. Dai, Acta Mater. 186 (2020) 257–266.
[37] Z. Pu, Y. Chen, L.H. Dai, Mater. Sci. Eng. A 736 (2018) 156–166.
[38] T. Yang, Y.L. Zhao, Y. Tong, Z.B. Jiao, J. Wei, J.X. Cai, X.D. Han, D. Chen, A. Hu, J.J. Kai, K. Lu, Y. Liu, C.T. Liu, Science 362 (6417) (2018) 933–937.
[39] P. Shi, R. Li, Y. Li, Y. Wen, Y. Zhong, W. Ren, Z. Shen, T. Zheng, J. Peng, X. Liang, P. Hu, N. Min, Y. Zhang, Y. Ren, P.K. Liaw, D. Raabe, Y.-D. Wang, Science 373 (6557) (2021) 912.
[40] Y.-Y. Tan, Z.-J. Chen, M.-Y. Su, G. Ding, M.-Q. Jiang, Z.-C. Xie, Y. Gong, T. Wu, Z.-H. Wu, H.-Y. Wang, L.-H. Dai, J. Mater. Sci. Technol. 104 (2022) 236–243.
[41] Z. Lei, X. Liu, Y. Wu, H. Wang, S. Jiang, S. Wang, X. Hui, Y. Wu, B. Gault, P. Kontis, D. Raabe, L. Gu, Q. Zhang, H. Chen, H. Wang, J. Liu, K. An, Q. Zeng, T.G. Nieh, Z. Lu, Nature 563 (7732) (2018) 546–550.

[42] Y. Yuan, Y. Wu, Z. Yang, X. Liang, Z. Lei, H. Huang, H. Wang, X. Liu, K. An, W. Wu, Z. Lu, Mater. Res. Lett. 7 (6) (2019) 225–231.
[43] H. Huang, Y. Wu, J. He, H. Wang, X. Liu, K. An, W. Wu, Z. Lu, Adv. Mater. 29 (30) (2017) 1701678.
[44] Y. Wu, F. Zhang, F. Li, Y. Yang, J. Zhu, H.-.H. Wu, Y. Zhang, R. Qu, Z. Zhang, Z. Nie, Y. Ren, Y. Wang, X. Liu, H. Wang, Z. Lu, Mater. Horiz. 9 (2) (2022) 804–814.
[45] Y. Lu, Y. Dong, H. Jiang, Z. Wang, Z. Cao, S. Guo, T. Wang, T. Li, P.K. Liaw, Scr. Mater. 187 (2020) 202–209.
[46] M. Wang, Y. Lu, T. Wang, C. Zhang, Z. Cao, T. Li, P.K. Liaw, Scr. Mater. 204 (2021) 114132.
[47] Y. Lu, Y. Dong, S. Guo, L. Jiang, H. Kang, T. Wang, B. Wen, Z. Wang, J. Jie, Z. Cao, H. Ruan, T. Li, Sci. Rep. 4 (1) (2014) 6200.
[48] Y. Lu, X. Gao, L. Jiang, Z. Chen, T. Wang, J. Jie, H. Kang, Y. Zhang, S. Guo, H. Ruan, Y. Zhao, Z. Cao, T. Li, Acta Mater. 124 (2017) 143–150.
[49] Y. Lu, X. Wu, Z. Fu, Q. Yang, Y. Zhang, Q. Liu, T. Li, Y. Tian, H. Tan, Z. Li, T. Wang, T. Li, J. Mater. Sci. Technol. 126 (2022) 15–21.
[50] X. Gao, Y. Lu, B. Zhang, N. Liang, G. Wu, G. Sha, J. Liu, Y. Zhao, Acta Mater. 141 (2017) 59–66.
[51] I.S. Wani, T. Bhattacharjee, S. Sheikh, Y.P. Lu, S. Chatterjee, P.P. Bhattacharjee, S. Guo, N. Tsuji, Mater. Res. Lett. 4 (3) (2016) 174–179.
[52] I.S. Wani, T. Bhattacharjee, S. Sheikh, P.P. Bhattacharjee, S. Guo, N. Tsuji, Mater. Sci. Eng. A 675 (2016) 99–109.
[53] P. Shi, W. Ren, T. Zheng, Z. Ren, X. Hou, J. Peng, P. Hu, Y. Gao, Y. Zhong, P.K. Liaw, Nat. Commun. 10 (1) (2019) 489.
[54] T. Xiong, S. Zheng, J. Pang, X. Ma, Scr. Mater. 186 (2020) 336–340.
[55] T. Xiong, W. Yang, S. Zheng, Z. Liu, Y. Lu, R. Zhang, Y. Zhou, X. Shao, B. Zhang, J. Wang, F. Yin, P.K. Liaw, X. Ma, J. Mater. Sci. Technol. 65 (2021) 216–227.
[56] L. He, S. Wu, A. Dong, H. Tang, D. Du, G. Zhu, B. Sun, W. Yan, J. Mater. Sci. Technol. 117 (2022) 133–145.
[57] Y. Guo, H. Su, H. Zhou, Z. Shen, Y. Liu, J. Zhang, L. Liu, H. Fu, J. Mater. Sci. Technol. 111 (2022) 298–306.
[58] I.N. Orbulov, Mater. Sci. Eng. A 583 (2013) 11–19.
[59] H. Lin, H.Y. Wang, C. Lu, L.H. Dai, Scr. Mater. 119 (2016) 47–50.
[60] ISO 13314: 2011 Mechanical testing of metals - Ductility testing - Compression test for porous and cellular metals, 2011.
[61] H. Kolsky, Proc. Phys. Soc. Sect. B 62 (11) (1949) 676–700.
[62] W. Weibin, S. Tao, G. Yazhou, L. Yulong, N. Hailiang, L. Huifang, J. Kanghua, D. Bin, J. Bin, Adv. Mech. 51 (4) (2021) 729–754.
[63] Y. Zhang, J. Li, X. Wang, Y. Lu, Y. Zhou, X. Sun, J. Mater. Sci. Technol. 35 (5) (2019) 902–906.
[64] D. Choudhuri, S. Shukla, P.A. Jannotti, S. Muskeri, S. Mukherjee, J.T. Lloyd, R.S. Mishra, Mater. Charact. 158 (2019) 109955.
[65] B. Zhang, Y. Lin, S. Li, D. Zhai, G. Wu, Compos. Part B-Eng. 98 (2016) 288–296.
[66] P.H. Thornton, C.L. Magee, Metall. Trans. A 6 (6) (1975) 1253–1263.
[67] K.C. Rusch, J. Appl. Polym. Sci. 14 (6) (1970) 1433–1447.
[68] S.K. Maiti, L.J. Gibson, M.F. Ashby, Acta Metall. 32 (11) (1984) 1963–1975.
[69] J. Miltz, G. Gruenbaum, Polym. Eng. Sci. 21 (15) (1981) 1010–1014.
[70] L. Pan, Y. Yang, M.U. Ahsan, D.D. Luong, N. Gupta, A. Kumar, P.K. Rohatgi, Mater. Sci. Eng. A 731 (2018) 413–422.
[71] G.A. Rocha Rivero, B.F. Schultz, J.B. Ferguson, N. Gupta, P.K. Rohatgi, J. Mater. Res. 28 (17) (2013) 2426–2435.
[72] J.A. Santa Maria, B.F. Schultz, J.B. Ferguson, N. Gupta, P.K. Rohatgi, J. Mater. Sci. 49 (3) (2014) 1267–1278.
[73] S. Broxtermann, M. Vesenjak, L. Krstulović-Opara, T. Fiedler, J. Alloy. Compd. 768 (2018) 962–969.
[74] S. Muskeri, V. Hasannaeimi, R. Salloom, M. Sadeghilaridjani, S. Mukherjee, Sci. Rep. 10 (1) (2020) 2669.
[75] M.F. Ashby, Philos. Mag. A 21 (170) (1970) 399–424.
[76] H. Gao, Y. Huang, Scr. Mater. 48 (2) (2003) 113–118.
[77] Z. Cheng, H. Zhou, Q. Lu, H. Gao, L. Lu, Science 362 (6414) (2018) eaau1925.
[78] L. Cui, C.-.H. Yu, S. Jiang, X. Sun, R.L. Peng, J.-.E. Lundgren, J. Moverare, J. Mater. Sci. Technol. 96 (2022) 295–307.
[79] T. Bhattacharjee, R. Zheng, Y. Chong, S. Sheikh, S. Guo, I.T. Clark, T. Okawa, I.S. Wani, P.P. Bhattacharjee, A. Shibata, N. Tsuji, Mater. Chem. Phys. 210 (2018) 207–212.
[80] Q. Xue, G.T. Gray, Metall. Mater. Trans. A 37 (8) (2006) 2447–2458.
[81] D. Rittel, P. Landau, A. Venkert, Phys. Rev. Lett. 101 (16) (2008) 165501.
[82] M.A. Meyers, V.F. Nesterenko, J.C. LaSalvia, Q. Xue, Mater. Sci. Eng. A 317 (1) (2001) 204–225.
[83] N. Yan, Z. Li, Y. Xu, M.A. Meyers, Prog. Mater. Sci. 119 (2021) 100755.
[84] X.H. Du, W.P. Li, H.T. Chang, T. Yang, G.S. Duan, B.L. Wu, J.C. Huang, F.R. Chen, C.T. Liu, W.S. Chuang, Y. Lu, M.L. Sui, E.W. Huang, Nat. Commun. 11 (1) (2020) 2390.
[85] L. Fan, T. Yang, Y. Zhao, J. Luan, G. Zhou, H. Wang, Z. Jiao, C.-.T. Liu, Nat. Commun. 11 (1) (2020) 6240.
[86] Z. Pu, Z.C. Xie, R. Sarmah, Y. Chen, C. Lu, G. Ananthakrishna, L.H. Dai, Philos. Mag. 101 (2) (2021) 154–178.
[87] M.A. Meyers, Y.B. Xu, Q. Xue, M.T. Pérez-Prado, T.R. McNelley, Acta Mater. 51 (5) (2003) 1307–1325.
[88] L.H. Dai, Z. Ling, Y.L. Bai, Compos. Sci. Technol. 61 (8) (2001) 1057–1063.
[89] X. Wei, J.H. Chen, L.H. Dai, Scr. Mater. 66 (10) (2012) 721–724.
[90] L. Zhang, Z. Liu, D. Jiao, J. Zhang, S. Wang, H. Zhang, Z. Zhang, J. Bionic Eng. 18 (3) (2021) 600–610.
[91] L.H. Dai, L.F. Liu, Y.L. Bai, Mater. Lett. 58 (11) (2004) 1773–1776.
[92] L.H. Dai, L.F. Liu, Y.L. Bai, Int. J. Solids Struct. 41 (22) (2004) 5979–5993.
[93] A.J. Ardell, Mater. Sci. Eng. A 152 (1) (1992) 212–226.